Scripta Materialia 161 (2019) 78–83

Contents lists available at ScienceDirect

Scripta Materialia

journal homepage: www.elsevier.com/locate/scriptamat

The effects of wide range of compositional changes on the martensitic transformation characteristics of NiTiHf shape memory alloys

Tejas Umale, Daniel Salas, Bradley Tomes, Raymundo Arroyave, Ibrahim Karaman *

Department of Materials Science and Engineering, Texas A&M University, College Station, TX 77843, USA

ARTICLE INFO

Article history:
Received 29 June 2018
Received in revised form 20 September 2018
Accepted 8 October 2018
Available online xxxx

Keywords:
NiTiHf
Martensitic phase transformation
High temperature shape memory alloy
Composition dependence

ABSTRACT

The effects of composition on the martensitic transformation characteristics of NiTiHf shape memory alloys are systematically explored. Transformation temperatures (TTs) demonstrate a non-monotonic dependence on Ni and Hf concentrations. For Ni > 50 at%, TTs decrease with small Hf additions, attain a minimum or are completely suppressed, depending on Ni content, followed by a significant increase with Hf content. This initial drop in TTs becomes more pronounced with higher Ni contents and is attributed to the increase in nickel anti-site defects along with bulky substitutional Hf contributing to the increase in local lattice distortions along with the redistribution of Ti and Hf.

Shape Memory Alloys (SMAs) have found limited utility in aerospace and energy applications despite their unusual mechanical and functional properties [1–5]. Among known SMAs, NiTi demonstrates the best combination of high transformation strain, high strength, and good thermal and dimensional stability [6]. However, applicability of NiTi is restricted below 100 °C because of the low martensitic transformation temperatures (TTs) [7]. The only known method to increase TTs in NiTi is the addition of Pt, Pd, Au, Zr, and Hf [7,8]. Pt, Pd, and Au are costly, while the known NiTiZr high temperature SMAs (HTSMAs) suffer from poor thermal stability, making Hf the most viable alloying element to increase the TTs [9–14]. NiTiHf HTSMAs have recently gained interest because of their wide range of TTs, which can be controlled by varying their compositions or through secondary heat treatments [14–24].

The shape memory characteristics of NiTiHf SMAs are highly composition dependent. When Ni ≤ 50 at%, NiTiHf alloys tend to have higher TTs, as compared to their Ni-rich counterparts, with comparatively lower strength, higher transformation hysteresis, and poor cyclic stability [7,13,25]. High strength, lower transformation hysteresis, and impressive cyclic stability in Ni-rich NiTiHf SMAs make them suitable for aerospace applications [20–22,26–28]. However, there is limited data available in literature which systematically presents the compositional dependence of MT characteristics of NiTiHf SMAs [8,16,17,34]. Previous works have only focused on narrow composition ranges (e.g. $Ni_{50.3}Ti_{49.7-X}Hf_X$ where X = 15,20 or 25 or Ni ≤ 50 at% compositions).

In this study, we seek to understand the role of composition on MT characteristics of NiTiHf SMAs by exploring the large portion of the compositional space that demonstrates MT. The composition of Ni was varied from 49.8 at% to 51.5 at% with Hf content ranging from 0 at% to 30 at%. Through this systematic study, we mapped the effect of nickel and hafnium on the martensite start temperature (Ms) and thermal hysteresis (Af-Ms) for solution heat treated NiTiHf alloys. As the composition of Ni and Hf are varied, Ti composition also changes correspondingly and has an influence on TTs. The results reported here emphasize the effects of variation in Ni and Hf contents on TTs, as the Hf dependence has not been studied systematically before and TTs are highly sensitive to Ni content variations in Ni-rich NiTiHf alloys. It was found that the TTs can be closely controlled between −170 °C to +500 °C in this composition range, which is the largest temperature window, to the best of our knowledge, systematically reported to date for MT in a single SMA system.

$Ni_XTi_{100-X-Y}Hf_Y$ alloy buttons (Ni_XTiHf_Y in what follows) were fabricated through vacuum arc melting of 10 g of 99.98% Ni, 99.99% Ti and 99.9% Hf (with <1%Zr) elements under high purity argon. The arc melting chamber was first pumped down to a pressure of 5×10^{-5} Torr or less, and then backfilled with ultra-high purity argon. This was repeated three times. The buttons were then remelted six times to reduce compositional heterogeneity. After the remelting steps, the weight loss was measured to be <0.10% in all cases that were selected for further characterization.

The buttons were wrapped in tantalum foils, sealed in quartz tubes under high purity argon, and solution heat treated (SHT) at 1050 °C for 2 h followed by water quenching. The TTs of the SHT buttons were determined using Differential Scanning Calorimetry (DSC) and Thermogravimetric Analysis (TGA), with a heating-cooling rate of 10 °C/min. For TTs less than −100 °C, the temperatures were determined from the temperature-dependence of the electrical resistivity, measured down to −263 °C, using a Quantum Design Physical Property

* Corresponding author.
E-mail address: ikaraman@tamu.edu (I. Karaman).

https://doi.org/10.1016/j.scriptamat.2018.10.008
1359-6462/

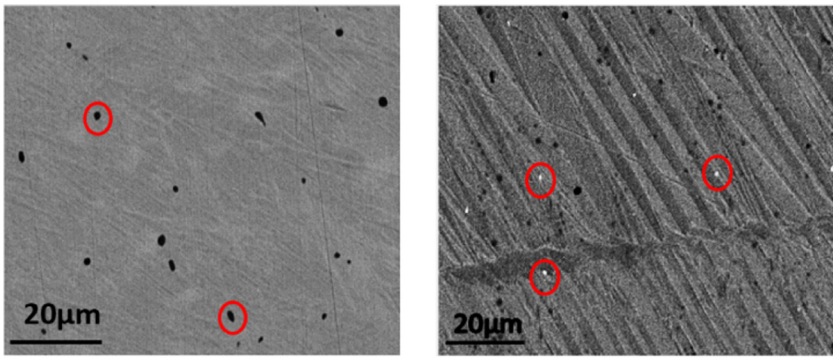

(a) (b)

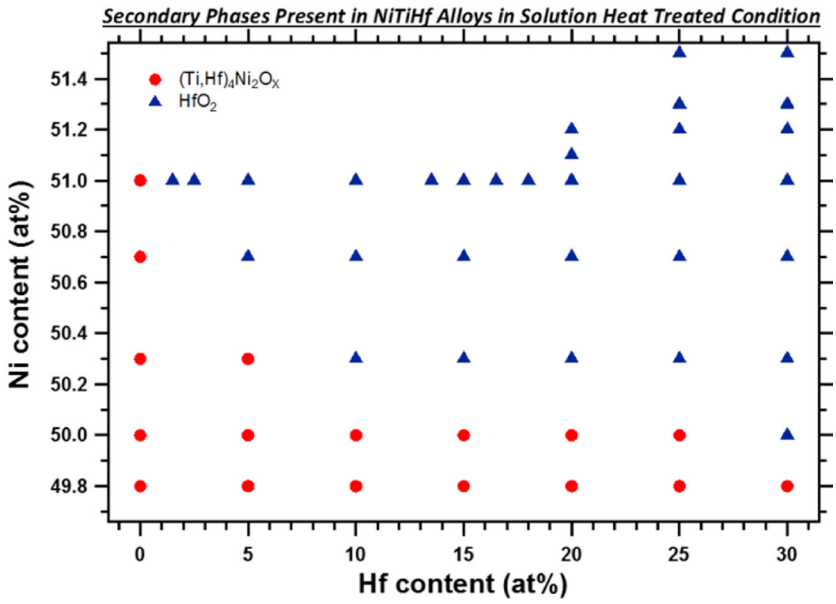

(c)

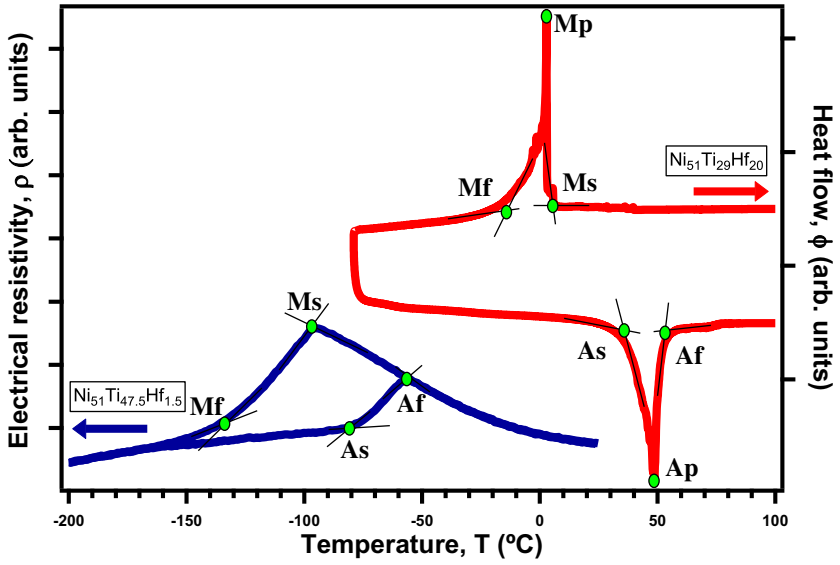

(d)

Fig. 1. Representative backscattered secondary electron (BSE) images to exemplify different phases observed in the solution heat treated NiTiHf alloys that demonstrate martensitic transformation: (a) $Ni_{49.8}Ti_{40.2}Hf_{10}$ showing $(Ti,Hf)_4Ni_2O_x$ particles marked with red circles in the martensite matrix; and (b) $Ni_{50.3}Ti_{24.7}Hf_{25}$ showing HfO_2 inclusions marked with red circles, again in martensite matrix. The black spots are surface contamination, which was also seen as bright spots in secondary electron image mode. (c) Phase map indicating the presence of B2 (austenite) or B19′ (martensite) matrix phase along with second phases observed in SEM, accurate down to micron scale. (d) shows representative DSC and PPMS plots for $Ni_{51}Ti_{29}Hf_{20}$ and $Ni_{51}Ti_{47.5}Hf_{1.5}$ alloys, respectively, depicting how the transformation temperatures were determined using two different methods. (For interpretation of the references to color in this figure legend, the reader is referred to the web version of this article.)

Measurement System (PPMS), with a heating-cooling rate of 2 °C/min. Scanning Electron Microscopy (SEM) was performed to observe the microstructure and search for possible second phases, compositions of which were analyzed, using a Cameca SXFive Electron Microprobe Analyzer (EPMA) using wavelength dispersive spectroscopy (WDS), operated at 15 KeV and 20 mA. The microstructure and diffraction patterns of the selected samples were obtained using an FEI Technai G2-F20 Transmission Electron Microscopy (TEM) operated at 200 kV. For TEM investigations, 3 mm diameter discs with 100 μm thickness were twin-jet electropolished using a 30%HNO_3 + 70% methanol solution at −20 °C under 10–12 V.

Microstructural characterization results of selected NiTiHf alloys are shown in Fig. 1. Fig. 1a displays the backscattered secondary electron (BSE) image of SHT $Ni_{49.8}TiHf_{10}$ showing martensite matrix and (Ti, Hf)$_4Ni_2O_x$ [18] particles marked with red circles. Fig. 1b displays the BSE image of SHT $Ni_{50.3}TiHf_{25}$ with martensite and HfO_2 inclusions marked with red circles. The results of these investigations performed on all samples are presented in the form of a phase map in Fig. 1c as a function of Ni and Hf contents. The map shows which other phases are observed in addition to austenite and martensite. The map was generated using the SEM microstructures, and hence is accurate down to the micron scale. Fig. 1d presents representative DSC and resistivity responses for $Ni_{51}Ti_{29}Hf_{20}$ and $Ni_{51}Ti_{47.5}Hf_{1.5}$ alloys, respectively, across MT during single cooling-heating cycles, demonstrating how the TTs are determined using these two methods.

TTs in NiTiHf alloys demonstrate a significant compositional dependence. Fig. 2a presents the Hf dependence of Ms for different Ni contents. For Ni-lean, Ni = 50 and 50.3at% compositions, Ms almost stays constant up to 5 to 10%Hf addition and increases drastically beyond 10% Hf. Previous reports on the Ni-lean compositions [8,16,17] present similar trends in Hf dependence of Ms. For Ni-rich compositions, Ms tends to initially decrease with increasing Hf, attaining a minimum, and then increase continuously. For Ni = 50.7 at% (Ni50.7), the Ms sharply decreased from 6 °C for 0%Hf to −66 °C for 10%Hf, where the minimum was attained. With further increase in Hf, Ms was found to increase. The DSC response of $Ni_{50.7}TiHf_{10}$ showed avalanche-like transformation behavior [30–33], while all other $Ni_{50.7}Ti_{49.3-Y}Hf_Y$ showed a single peak B2 → B19′ MT. For Ni = 51at%, the initial drop in Ms with Hf content was more pronounced than Ni50.7 alloys, from −22 °C for 0%Hf to −96 °C for 1.5at%Hf. However, $Ni_{51}TiHf_5$, $Ni_{51}TiHf_{10}$, and $Ni_{51}TiHf_{15}$ didn't undergo MT down to −260 °C and this is indicated in Fig. 2a as a dashed line disappearing at the bottom of the figure. Here, the solid lines are for guiding the eyes, connecting the compositions that show complete MT, while the dashed lines link transforming and non-transforming compositions.

To better reveal the compositional boundary for the full suppression of MT in Ni51 alloys, $Ni_{51}TiHf_{2.5}$, $Ni_{51}TiHf_{16.5}$ and $Ni_{51}TiHf_{18}$ alloys were also prepared. PPMS measurements for $Ni_{51}TiHf_{2.5}$ and $Ni_{51}TiHf_{16.5}$ demonstrate no MT. The DSC result of $Ni_{51}TiHf_{18}$ exhibits many sharp, discrete transformation peaks, indicating avalanche-like transformation bursts [30–33]. MT can occur in the form of avalanches, if there are barriers to MT which tend to pin down the transformation front. With the higher degree of undercooling/overheating, when the system has enough driving force to overcome the barriers, the transformation can proceed until obstructed again by new barriers, and hence advancing in the form of bursts.

For Ni51.2 alloys, in addition to $Ni_{51.2}TiHf_0$, 3 other compositions were fabricated with Hf contents ranging from 20% to 30at%, where the samples are expected to transform. Firstly, the Ms increases with Hf content similar to the previous cases within this high Hf range. Secondly, when MT occurred at low temperatures in $Ni_{51.2}TiHf_{20}$ and $Ni_{51.2}TiHf_{25}$ alloys, the transformations displayed avalanche-like transformation features in DSC, whereas $Ni_{51.2}TiHf_{30}$ alloy experienced a single peak MT.

To better understand the effect of Ni on TTs and compare the Ni dependence of NiTiHf alloys to that of binary NiTi, Fig. 2b is constructed as a function of Ni using constant Hf curves. For Hf ≤ 25% alloys, Ms is roughly independent of Ni-content for Ni ≤ 50%. However, above 50% Ni, Ms exhibits a non-linear, inverse dependence on Ni content which becomes steeper with increasing Ni beyond 51%. This trend is similar to binary NiTi [29] and initial compositional studies performed on NiTiHf SMAs by Abu Judom et al. [16] which also depicted that the TTs didn't change with increase in Ni ≤ 50 at% (attaining a plateau) followed by steep decrease in TTs for Ni ≥ 50 at%. In the present work, since only alloys with Ni ≥ 49.8 at% were prepared, Fig. 2b mainly shows the region of steep decrease in TTs. If the length scale on X-axis would be changed to accommodate more Ni-lean compositions, then the trendlines in Fig. 2b would also show a similar plateau for Ni ≤ 50 at%, followed by steep decrease beyond Ni ≥ 50 at%. For 30%Hf, no appreciable change in Ms was observed up to Ni = 50.7%, but Ms started decreasing very rapidly beyond Ni = 50.7%. Hence, the degree of the Ms dependence on the amount of excess Ni required to fully suppress MT depends on Hf content. For example, Ni = 51% is sufficient to suppress MT for Hf = 10% alloys, whereas Ni = 51.5% is required to suppress MT for Hf = 20,25 and 30%.

Fig. 2c presents the Hf dependence of the transformation hysteresis (Af-Ms) for different nickel contents, exhibiting a strongly non-monotonic behavior. With increasing Hf, the hysteresis tends to increase and attain a maximum around Hf = 8–11%, (which coincides with the Ms minimum), and then a minimum around Hf = 20%. Beyond Hf = 20%, MT hysteresis increases again, however it displays stronger Ni dependence and larger scattering as compared to the lower Hf contents. Nevertheless, the results indicate that Ni-rich compositions exhibit larger hysteresis than Ni-lean compositions for Hf ≥ 20%.

TTs presented here are higher than the ones reported in the literature for the most commonly studied alloys such as $Ni_{50.3}TiHf_{20}$ and $Ni_{50.3}TiHf_{15}$ [15,34]. This is because of the fact that only nominal compositions are reported in the literature, and most of these alloys were manufactured in large quantities using vacuum induction or skull melting techniques. During melting with these methods, a considerable amount of Hf/Ti is lost because of oxidation and/or carbide formation, hence, increasing the real nickel content of the alloy. The compositional measurements using the inductively coupled plasma atomic emission spectroscopy (ICP-AES) on some of these $Ni_{50.3}TiHf_x$ samples revealed Ni contents to range between 50.7 and 51.4 at%. However, those measurements consist of relatively large uncertainties from the ICP-AES measurements. A recent study conducted by Benafan et al. [34] showed that the degree of the scatter associated with ICP-AES measurements for Ni can range close to 1 at%, which could change TTs over 300 °C depending on the Hf content. In the present study we only used samples where the weight loss during melting was <0.10%, and we therefore believe the current results are reasonably accurate.

Analysis of the above results leads to the observation of few interesting phenomena related to the MT characteristics in NiTiHf alloys. Although it has been known that Hf, replacing Ti, increases the TTs of NiTi alloys [16–18], how off-stoichiometric Ni contents influence the change in TTs has not been systematically studied. It is clear from Fig. 2b that excess Ni leads to significant changes in TTs, yielding Ms variations as large as 500 °C for a given Hf content, through a change in Ni from 50at% to 51.3 at%. Such dependence of TTs in excess Ni in NiTiHf alloys is more pronounced as compared to the 83 °C change in Ms with 1 at% excess Ni in NiTi [29]. Secondly, the rapid reduction of TTs and complete suppression of MT with small Hf additions in Ni-rich NiTi alloys have not been reported before and are somewhat unexpected. These results indicate that, along with Ni anti-site defects in Ti sublattice, which lead to drop in TTs in binary NiTi [8,29], bulky Hf atoms replacing Ti should contribute to the increase in local lattice distortions, and thus, the reduction in TTs in NiTiHf alloys. In addition, the cumulative increase in local lattice distortions is likely to stabilize the quasi-dynamic strain nano-domains in austenite, similar to those reported for Ni-rich NiTi and NiTiFe systems [35–37]. These defects tend to hinder MT, causing energy barriers to the nucleation and growth of

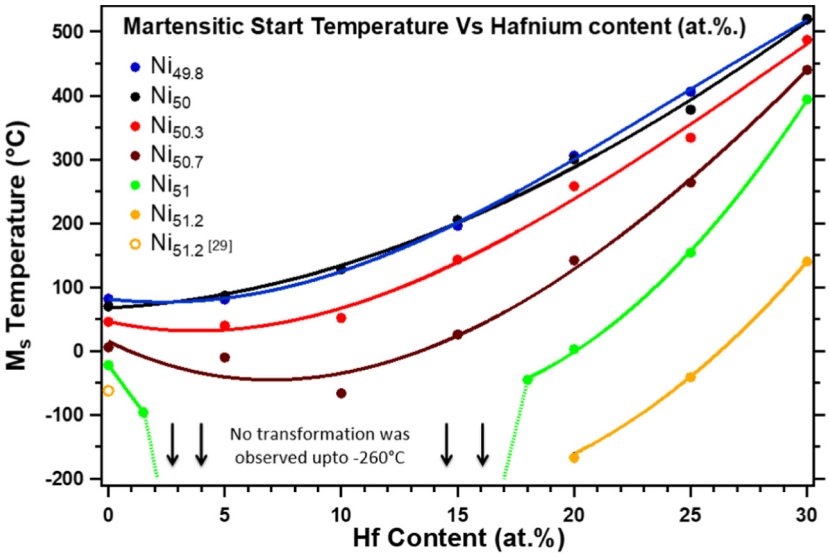

(a)

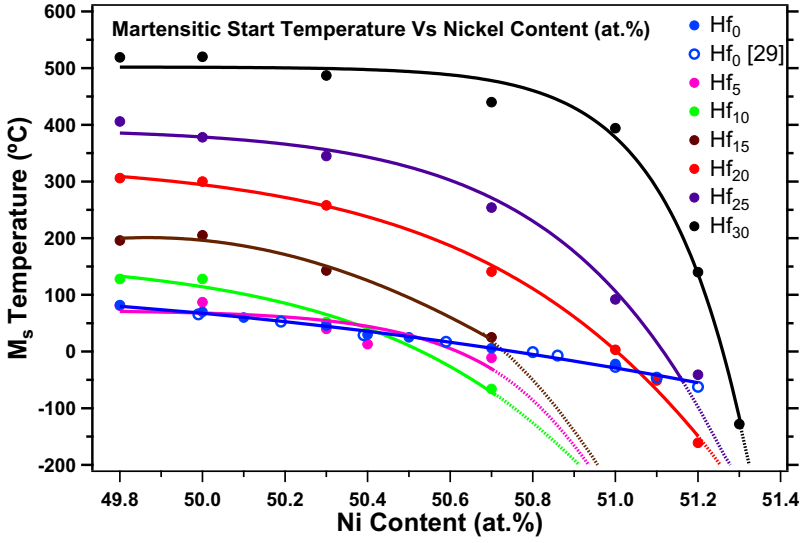

(b)

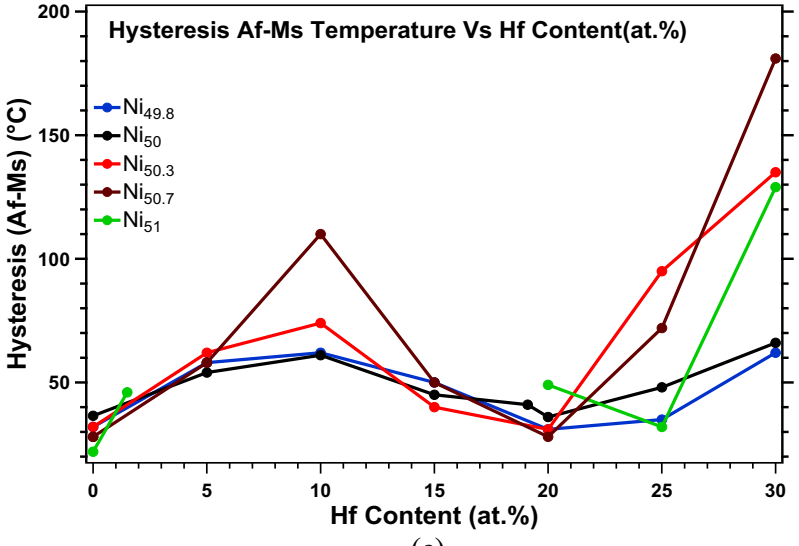

(c)

Fig. 2. (a) Variation of Ms temperatures with hafnium content for various NiTiHf alloys for selected Ni contents; (b) variation of Ms temperatures with nickel content for constant Hf contents; and (c) variation of transformation hysteresis (Af-Ms) vs. Hf content for the same samples. Solid and dashed lines serve as a guide to the eye.

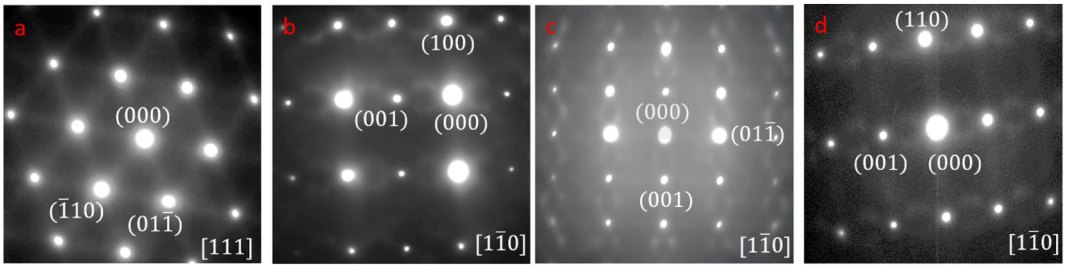

Fig. 3. Selected area electron diffraction patterns (SAEDPs) obtained from (a) $Ni_{50.7}TiHf_{10}$ along $[111]_{B2}$ showing diffuse scattering along ⟨110⟩ directions; (b) $Ni_{51}TiHf_5$ and (c) $Ni_{51}TiHf_{10}$ along $[1\bar{1}0]_{B2}$ showing diffuse scattering along ⟨001⟩ direction, while (d) $Ni_{51}TiHf_{15}$ along $[1\bar{1}0]_{B2}$ which displays diffuse scattering along ⟨001⟩ and ⟨110⟩ directions. These diffuse scattering patterns are attributed to the short range ordering due to the redistribution between Ti and Hf atoms.

martensite. As the consequence, amount of overcooling required for the onset of transformation increases, and hence Ms decreases. This hypothesis can be proven with electronic structure calculations, seeking for the role of Hf on the Fermi surface nesting responsible for MT, however, such calculations would be computationally expensive due to the size of the supercells needed to mimic the off-stoichiometric compositions.

Another effect of Ni and Hf substitutional defects on MT of NiTiHf alloys is that the degree of transformation arrest changes between alloys undergoing normal MTs and the ones showing no transformation, depending on the Ni and Hf concentrations. From Fig. 2a and b it can be seen that TTs notably decrease for Hf-contents around 8–11% and with increase of excess Ni. The dependence of TTs and hysteresis on Hf is non-monotonic showing an Ms minimum and a hysteresis maximum around these compositions. At the same time, Hf substitutions lead to an increase in the lattice parameter of the austenite, especially for Hf-contents beyond 10%, causing overall expansion of the unit cell. Therefore, the local lattice distortions caused by few Hf atoms start decreasing as a result of overall expansion of the unit cell at higher Hf contents [41]. Due to the reduction in the lattice distortions, barriers to B2 → B19′ transformation decrease and MT is recovered, causing an increase in TTs and decrease in hysteresis. On the other hand, Fig. 2c depicts a minimum for MT hysteresis around Hf = 20% for all Ni contents, and notable increase in the hysteresis beyond 20% Hf. The origin of this increase in the hysteresis with Hf beyond 20% is not clear.

Fig. 3 shows the room temperature selected area electron diffraction patterns (SAEDPs) of the NiTiHf alloys with fully suppressed MT. All SAEDPs exhibit characteristic primary reflections spots of the B2 austenite. Fig. 3a depicts the SAEDP from $Ni_{50.7}TiHf_{10}$ along $[111]_{B2}$ which shows diffuse scattering along ⟨110⟩ direction. Fig. 3b and c display the SAEDPs from $Ni_{51}TiHf_5$ and $Ni_{51}TiHf_{10}$ along $[001]_{B2}$, respectively, which feature similar intense diffuse scattering along ⟨100⟩ direction. Fig. 3d exhibits the SAEDP along $[1\bar{1}0]_{B2}$ from $Ni_{51}Ti_{34}Hf_{15}$, with diffuse scattering along both ⟨001⟩ and ⟨110⟩ directions. Saghaian et al. [20] and Coughlin et al. [42] observed similar diffuse scattering in ⟨001⟩ and ⟨$\bar{1}$10⟩ SAEDPs in SHT $Ni_{51.2}Ti_{28.8}Hf_{20}$ and as extruded $Ni_{51}Ti_{28.8}Hf_{20}$, respectively. Sandu et al. [38,39] conducted extensive TEM studies on $Ni_{52}TiZr_6$ and $Ni_{53}TiZr_6$ reporting that the diffuse scattering can be attributed to segregation and short range ordering (SRO) of Zr atoms (Hf in our case, NiTiZr system is similar to NiTiHf [28,40]). These diffuse streaks in diffraction patterns are attributed to the redistribution between Ti and Hf or Zr atoms, which can act as a precursor state to the formation of H-phase nano-precipitates, as proposed by Pérez-Sierra et al. [12]. Coughlin et al. [42] observed ~5 nm sized high intensity areas showing characteristic $n/4(111)_{B2}$ superlattice spots in the Fast Fourier Transform (FFT) obtained from the high resolution scanning TEM images, which they defined as H′ phase, that is the precursor to the H-phase. It is believed that the SRO creates elastic barriers to the transformation, contributing to the reduction of TTs and suppression of MT in the present compositions. The compositions considered here were solutionized and water quenched without any additional heat treatment. This suggests that the kinetics for the segregation of Ti and Hf atoms must be fast such that diffuse streaks in SAEDPs appear and MT is hindered. For Hf = 10%, the reduction in Ms is enhanced with increasing Ni-content, which indicates that higher the Ni-content is, higher the degree of SRO for Hf atoms might be. One possible reason for the increase in SRO with increasing Ni can be the excessive increase in local strains within the unit cell [8].

In summary, transformation temperatures of NiTiHf SMAs can be tailored over a wide range of temperatures ranging from −170 °C up to 500 °C by varying nickel (49.8 to 51.5 at%) and hafnium (0 to 30at %). For Ni-lean and Ni = 50 at% compositions, the TTs didn't increase much with Hf addition up to 10% followed by continuous increase of TTs beyond 10%. For Ni-rich compositions, TTs decreased with initial Hf addition attaining a minimum followed by continuous increase. This initial drop of TTs can be attributed to the local lattice distortions created by nickel anti-site and hafnium substitutional defects which tend to stabilize austenite and cause frozen strain nanodomains in B2 austenite. One more contributing factor for lowering of TTs can be the short range ordering between Ti and Hf atoms in the Ti sublattice which can act as a precursor to H-phase nanoprecipitates. Dynamic mechanical analysis and high resolution TEM need to be conducted on the specimens to gather additional evidences for the aforementioned phenomena.

Acknowledgements

This work is supported by Designing Materials to Revolutionize and Engineer our Future (DMREF) Program under National Science Foundation (NSF) Grant no. 1534534 and the NASA University Leadership Initiative Grant Number NNX17AJ96A. Authors thank Dr. Ruben Santamarta for discussions on the H-phase precursors and William Trehern, Dr. Abhishek Pandey and Dr. Omprakash Shukla for PPMS measurements.

References

[1] J. Mohd Jani, M. Leary, A. Subic, M. Gibson, Mater. Des. 56 (2014) 1078–1113.
[2] D.J. Hartl, D.C. Lagoudas, J. Aerosp. Eng. 221 (2007) 535–552.
[3] S. Miyazaki, A. Ishida, Mater. Sci. Eng. A 273–275 (1999) 106–133.
[4] M. Geetha, A. Singh, R. Asokamani, A. Gogia, Prog. Mater. Sci. 54 (2009) 397–425.
[5] N. Morgan, Mater. Sci. Eng. A 378 (2004) 16–23.
[6] K. Otsuka, X. Ren, Prog. Mater. Sci. 50 (2005) 511–678.
[7] J. Ma, I. Karaman, R.D. Noebe, Int. Mater. Rev. 55 (2010) 257–315.
[8] J. Frenzel, A. Wieczorek, I. Opahle, B. Maaß, R. Drautz, G. Eggeler, Acta Mater. 90 (2015) 213–231.
[9] S. Besseghini, E. Villa, A. Tuissi, Mater. Sci. Eng. A 273 (1999) 390–394.
[10] S. Hsieh, S. Wu, Mater. Charact. 41 (1998) 151–162.
[11] X. Meng, Y. Tong, K. Lau, W. Cai, L.M. Zhou, L.C. Zhao, Mater. Lett. 57 (2002) 452–456.
[12] A. Pérez-Sierra, J. Pons, R. Santamarta, I. Karaman, R.D. Noebe, Scr. Mater. 124 (2016) 47–50.
[13] B. Kockar, I. Karaman, J. Kim, Y. Chumlyakov, Scr. Mater. 54 (2006) 2203–2208.
[14] H. Karaca, S. Saghaian, G. Ded, H. Tobe, B. Basaran, H. Maier, R.D. Noebe, Y. Chumlyakov, Acta Mater. 61 (2013) 7422–7431.
[15] A. Evirgen, I. Karaman, R. Santamarta, J. Pons, R.D. Noebe, Acta Mater. 83 (2015) 48–60.

[16] D. Abu Judom, P. Thoma, M. Kao, D. Angst, US Patent No. 5114504 (1992).
[17] D. Angst, P. Thoma, M. Kao, J. Phys. IV (5) (1995) 747–752.
[18] P. Olier, J. Brachet, J. Bechade, C. Foucher, G. Guénin, J. Phys. IV (5) (1995) 741–746.
[19] B. Hornbuckle, T. Sasaki, G. Bigelow, R.D. Noebe, M. Weaver, G. Thompson, Mater. Sci. Eng. A 637 (2015) 63–69.
[20] S. Saghaian, H. Karaca, H. Tobe, J. Pons, R. Santamarta, Y. Chumlyakov, R.D. Noebe, Smart Mater. Struct. 25 (2016) 095029.
[21] G.S. Bigelow, A. Garg, S.A. Padula II, D.J. Gaydosh, R.D. Noebe, Scr. Mater. 64 (2011) 725–728.
[22] O. Karakoc, C. Hayrettin, M. Bass, S.J. Wang, D. Canadinc, J.H. Mabe, D.C. Lagoudas, I. Karaman, Acta Mater. 138 (2017) 185–197.
[23] A. Evirgen, F. Basner, I. Karaman, R.D. Noebe, J. Pons, R. Santamarta, Funct. Mater. Lett. 5 (2012) 1250038.
[24] A. Evirgen, J. Pons, I. Karaman, R. Santamarta, R.D. Noebe, Shape Mem. Superelast. 4 (2018) 85–92.
[25] D. Canadice, W. Trehern, H. Ozcan, C. Hayrettin, O. Karakoc, I. Karaman, F. Sun, Z. Chaudhry, Scr. Mater. 135 (2017) 92–96.
[26] S. Saghaian, H. Karaca, H. Tobe, A. Turabi, S. Saedi, S. Saghaian, R.D. Noebe, Acta Mater. 134 (2017) 211–220.
[27] A. Stebner, G. Bigelow, J. Yang, D. Shukla, S. Saghaian, R. Rogers, A. Garg, H. Karaca, Y. Chumlyakov, K. Bhattacharya, R.D. Noebe, Acta Mater. 76 (2014) 40–53.
[28] R. Santamarta, R. Arróyave, J. Pons, A. Evirgen, I. Karaman, H. Karaca, R.D. Noebe, Acta Mater. 61 (2013) 6191–6206.
[29] J. Frenzel, E. George, A. Dlouhy, C. Somsen, M. Wagner, G. Eggeler, Acta Mater. 58 (2010) 3444–3458.
[30] V. Hardy, S. Hebert, A. Maignan, C. Martin, M. Hervieu, B. Raveau, J. Magn. Magn. Mater. 264 (2003) 183–191.
[31] E. Vives, J. Ortin, L. Manosa, I. Rafols, R. Perez-Magrane, A. Planes, Phys. Rev. Lett. 72 (1994) 1694–1697.
[32] A. Planes, E. Vives, J. Phys. Condens. Matter 29 (2017) 334001.
[33] D.L. Beke, M.K. Bolgár, L.Z. Tóth, L. Daróczi, J. Alloys Compd. 741 (2018) 106–115.
[34] O. Benafan, G. Bigelow, D. Scheiman, Scr. Mater. 146 (2018) 251–254.
[35] S. Sarkar, X. Ren, K. Otsuka, Phys. Rev. Lett. 95 (2005) 205702.
[36] Z. Zhang, Y. Wang, D. Wang, Y. Zhou, K. Otsuka, X. Ren, Phys. Rev. B 81 (2010) 224102.
[37] D. Wang, Z. Zhang, J. Zhang, Y. Zhou, Y. Wang, X. Ding, Y. Wang, X. Ren, Acta Mater. 58 (2010) 6206–6215.
[38] A. Sandu, K. Tsuchiya, M. Tabuchi, S. Yamamoto, Y. Todaka, M. Umemoto, Mater. Trans. 48 (2007) 432–438.
[39] A. Sandu, S. Yamamoto, Y. Todoka, M. Umemoto, K. Tsuchiya, M. Saito, T. Hara, Y. Matsui, Proc. Shape Mem. Superelast. Technol. (2008) 101–108.
[40] A. Evirgen, I. Karaman, R. Santamarta, J. Pons, C. Hayrettin, R.D. Noebe, Acta Mater. 121 (2016) 374–383.
[41] M. Zarinejad, Y. Liu, T. White, Intermetallics 16 (2008) 876–883.
[42] D. Coughlin, L. Casalena, F. Yang, R.D. Noebe, M. Mills, J. Mater. Sci. 51 (2016) 766–778.